

# SMOV: COS NUV Imaging Performance

---

Paul Goudfrooij<sup>1</sup>, Eric Burgh<sup>2</sup>, Alessandra Aloisi<sup>1</sup>, George Hartig<sup>1</sup>, and Steven Penton<sup>2</sup>

<sup>1</sup> Space Telescope Science Institute, Baltimore, MD

<sup>2</sup> Center for Astrophysics and Space Astronomy, University of Colorado, Boulder, CO

7 October 2010

---

## ABSTRACT

*We describe the COS NUV imaging performance as derived from SMOV4 data. This includes photometric growth curves using data taken with the two available MIRROR settings (MIRRORA and MIRRORB) and the PSA and BOA apertures, throughput and image quality as function of spatial offset from the center of the COS aperture, and a description of the imaging-mode point spread function (PSF). The model PSF compares very well with the observed one, except for two minor ghosts located about 20 pixels away from the PSF center. A comparison of imaging observations of a cool and a hot flux standard star reveals a significantly higher red sensitivity of the COS imaging modes than that predicted from ground calibration data. New MIRROR throughput curves were therefore derived and delivered to SYNPHOT. These throughput curves are used in the COS imaging and imaging target acquisition exposure time calculators since October 7, 2009. Image drift during 5 HST orbits was determined from centroids of WCA exposures. The drift is dominated by movement in the X direction. The drift amplitude is significant: ~3.5 pixels with an e-folding time of ~50 min. With this in mind, observers taking images with exposure times longer than ~200 s are urged to use the TIME-TAG operating mode with the FLASH optional parameter.*

## **Contents:**

- Introduction (page 2)
- COS Imaging Modes (page 2)
- Data (page 3)
- The COS Point Spread Function (page 4)
- Photometric Analysis (page 6)
- Image Drift During 5 Orbits of Data Taking (page 15)
- Image-mode Plate Scale and Orientation (page 15)
- Change History for COS ISR 2010-10 (page 16)
- References (page 16)

## **1. Introduction**

This report addresses the performance of the NUV imaging modes available for the COS instrument as measured from the Servicing Mission Orbital Verification (SMOV) tests performed in the few months after the successful HST Servicing Mission 4 in May 2009. This report is organized as follows. After a brief description of the available COS imaging modes in §2, we present the data used in our analysis as well as relevant features of the targets in the context of flux calibration in §3. §4 describes relevant features of the COS Point Spread Function (PSF), while §5 presents photometry of the COS imaging modes and its dependences on measurement aperture size, location within the COS aperture, and breathing/focus changes. §5 also describes a re-determination of the imaging mode throughput curves. §6 describes the image drift properties during several HST orbits. Finally, §7 describes the determination of the imaging plate scale and its orientation with respect to the HST coordinate system.

## **2. COS Imaging Modes**

COS imaging observations can use either MIRRORA or MIRRORB. These use actually the same physical component, but two different angles of incidence: Either a reflection from the Al/MgF<sub>2</sub>-coated plane mirror (MIRRORA), or from a (tilted) “order sorting” filter of fused silica that is mounted in front of that mirror (MIRRORB) is imaged on the detector. MIRRORA has the higher throughput and cleaner image, and can be expected to serve as the main imaging mode used within COS. However, it does feature a short-wavelength cutoff to its throughput, caused by the fused silica substrate of the aforementioned filter. The MIRRORB mode does not have this short-wavelength cutoff. Both mirror settings can be used in conjunction with two different apertures (both of which have a diameter of 2.5 arcsec): The Primary Science Aperture (PSA) and the Bright Object Aperture (BOA). The latter includes a ND2 neutral density filter and features a wedge shape that degrades the image quality (see §4 and Chapters 3.3

and 8.4 of the COS Instrument Handbook). The BOA is mainly used for target acquisition of objects that are too bright to be imaged with the PSA.

### 3. Data

The data used in this report were acquired during visits 1 and 2 of HST Program 11473. A list of exposures is shown in Table 1. To enable a proper initial on-orbit flux calibration for the COS imaging modes, the targets comprised two HST flux standard stars with widely different spectral energy distributions (SEDs):

- 1) The solar-type (G2V) star P330E for which a high-quality HST reference spectrum is available from 2000 – 24440 Å, using STIS, FOS, and NICMOS spectrophotometry (Colina & Bohlin 1996; Bohlin, Riess, & de Jong 2006).
- 2) The DBQ4 star LDS749B (Bohlin et al. 1990; Bohlin et al. 2006; Bohlin & Koester 2008), a relatively cool white dwarf star with  $T_{\text{eff}} = 13,575$  K for which the HST reference spectrum covers 1150 – 24960 Å.

As the short-wavelength cutoff of the throughput curves of both MIRRORA and MIRRORB is shortward of the shortest wavelength covered by the P330E reference spectrum, we supplemented the latter in the 1200 – 2000 Å region by a scaled version of the Solar spectrum of Colina et al. (1996). Note that the radiation of solar-type stars below 2000 Å is dominated by chromospheric emission which undergoes variations associated with the solar activity cycle and rotation period. Variations of up to  $\pm 15\%$  are known to occur for the Sun in the 1500 – 2000 Å interval (Woods et al. 1996). However, the low sensitivity of the COS MAMA in this wavelength regime renders the systematic uncertainty caused by this variation negligible in the context of the following photometric analyses (specifically,  $\leq 0.25\%$  in MIRRORA throughput and  $\leq 0.30\%$  in MIRRORB throughput). The SEDs of the two targets are shown in Figure 1.

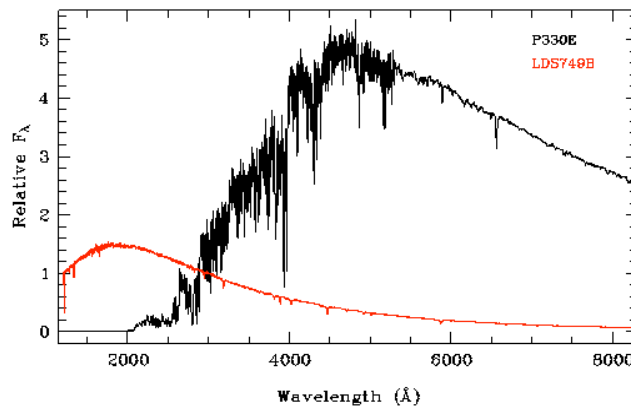


**Figure 1:** Spectral Energy Distributions (SEDs) of the two target flux standard stars P330E (black line) and LDS749B (red line). The two SEDs were normalized to unity at a wavelength of 3000 Å to facilitate the comparison.

**Table 1: List of exposures used in this report.**

Target	Rootname	Aperture	Spectral Element	Oper. Mode	Exp. Time (s)	POS TARG	Comments
WAVE	laa701a2q	WCA	MIRRORA	TIME-TAG	20	[0,0]	Wavecal exposure
P330E	laa701a4q	PSA	MIRRORA	TIME-TAG	450	0,0	TAG-FLASH mode
WAVE	laa701a6q	WCA	MIRRORA	TIME-TAG	20	[0,0]	Wavecal exposure
P330E	laa701a8q	PSA	MIRRORA	TIME-TAG	900	0,0	FLASH mode
WAVE	laa701aaq	WCA	MIRRORA	TIME-TAG	20	[0,0]	Wavecal exposure
P330E	laa701acq	PSA	MIRRORA	ACCUM	60	Various	45 exp's covering central 1.5 x 1.5 arcsec <sup>2</sup> , wavecal interspersed
(and WAVE)	laa701cwq						
P330E	laa701cyq	PSA	MIRRORB	TIME-TAG	475	0,0	TAG-FLASH mode
WAVE	laa701d0q	WCA	MIRRORA	TIME-TAG	20	[0,0]	Wavecal exposure
LDS749B	laa702acq	PSA	MIRRORB	ACCUM	60	0,0	
LDS749B	laa702afq	BOA	MIRRORA	ACCUM	80	0,0	
LDS749B	laa702atq	BOA	MIRRORA	ACCUM	80	0,0	
LDS749B	laa702b7q	BOA	MIRRORA	ACCUM	80	0,0	
LDS749B	laa702bpq	BOA	MIRRORA	ACCUM	80	0,0	
LDS749B	laa702c9q	BOA	MIRRORB	TIME-TAG	2630	0,0	

#### 4. The COS Point Spread Function

We created model imaging-mode PSFs at wavelengths of 170 - 320 nm using steps of 10 nm, incorporating the geometry of the HST Optical Telescope Assembly (OTA), including the 18 nm RMS wavefront error due to zonal errors of the OTA mirrors (Krist & Burrows 1995; Ghavamian et al. 2009) and an estimate (15 nm RMS) of the mean low-frequency wavefront error at the COS focus. The resultant PSF was then convolved with the known blur function of the STIS NUV-MAMA detector (note that the COS MAMA is the flight spare of the latter).

Using the long exposure of target P330E with root name laa701a8q (cf. Table 1), we show an empirical PSF in Figure 2. Note the two low-level “ghost” images which are located about 20 pixels to the right and upper left from the center of the PSF. The peak intensity of the brightest of the two ghosts is about 0.1% of that of the PSF center.

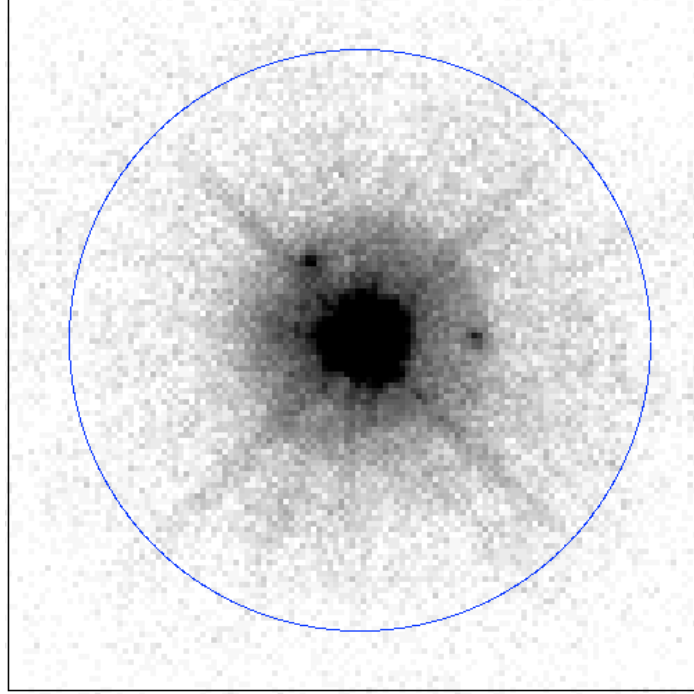


**Figure 2:** Negative greyscale rendering of inner  $3 \times 3$  arcsec<sup>2</sup> of a deep PSA/MIRRORA image of P330E. The image is plotted with a logarithmic intensity scale. Note the two ghost images located about 0.5 arcsec (20 pixels) to the right and upper left of the PSF center. The nominal COS aperture (with a radius of 1.25 arcsec) is shown as a blue circle.

Since the effect of the mid-frequency wavefront errors to the PSF weakens with increasing wavelength, the shape of the imaging PSF is expected to depend on the SED of the target to some extent. To explore the significance of this effect, we created simulated PSFs for the two targets used in this program (i.e., the cool star P330E and the hot star LDS749B) by first folding their known SEDs through the throughput curves of the PSA/MIRRORA and PSA/MIRRORB observing modes (these throughput curves are described in detail in §5.1 below), and using the resulting “effective SEDs” to derive weighting factors as a function of wavelength. The latter were then used to create “effective imaging PSFs” from the model PSFs. The resulting simulated imaging PSFs for P330E and LDS749B are shown in the left panel of Figure 3 after averaging over  $180^\circ$  of azimuth. To compare model with observation, the right panel of Figure 3 compares the model PSF for P330E with the empirical one by averaging Figure 2 over  $180^\circ$  of azimuth. The model PSF obviously provides a good description of the empirical one (except around the radii where the ghosts are located, cf. Figure 2).

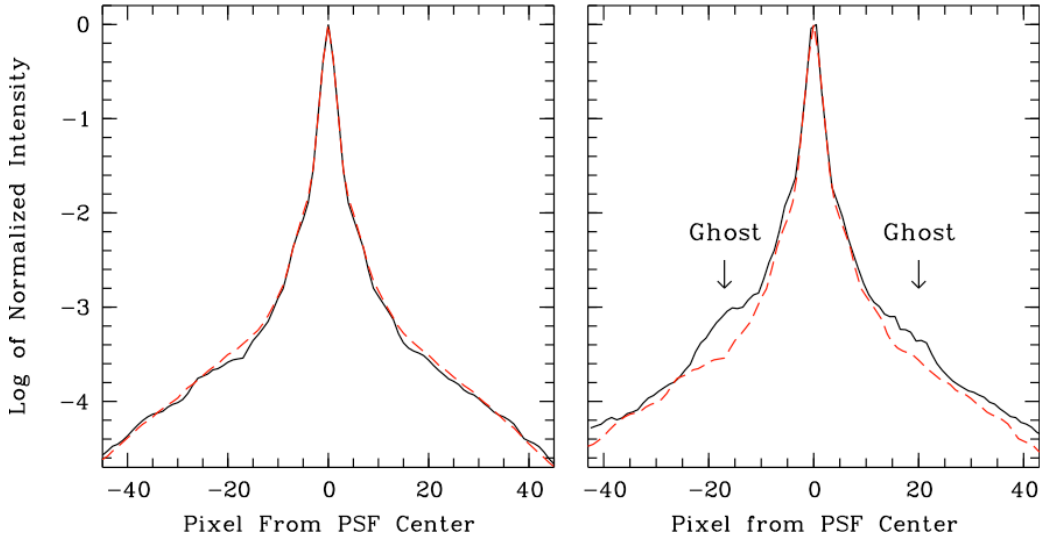


**Figure 3.** *Left panel:* Simulated COS PSFs for target/mirror combinations P330E/MIRRORA (black solid line) and LDS749B/MIRRORB (red dashed line; see §4 for details). *Right panel:* Comparison of observed azimuth-averaged PSF (black solid line) with simulated azimuth-averaged PSF for target P330E in PSA/MIRRORA configuration (red dashed line). The location of the two ghosts in Figure 2 are indicated for reference.

## 5. Photometric Analysis

We used the DAOPHOT photometry package as implemented within IRAF for the photometric growth curve analysis. For MIRRORA data, aperture photometry was conducted using the `phot` task for aperture radii of 0.5, 1, 2, 3, 5, 7, 10, 20, 40, and 60 pixels. For MIRRORB data, the finite thickness of the order-sorting filter on the mirror causes a secondary image that contains about 45% of the flux in the primary image, and is located about 20 pixels away from it (see Chapter 8.4.2 of the COS Instrument Handbook). Hence we chose the largest measurement aperture radius for MIRRORB data to be 10 pixels (for the primary image). Target centering within the measurement aperture was performed by means of intensity-weighted averages of the  $x$  and  $y$  profiles. Given the presence of extended wings in the COS NUV point spread function (cf. §4), the sky background was determined within a circular annulus with an inner radius of 60 pixels and a width of 10 pixels.

### 5.1. Photometry at center of PSA aperture

Results of the growth curve analysis for all PSA exposures of target P330E that were taken at the nominal center of the PSA aperture are shown in Figure 4 and listed in Table 2. The photometry in Table 2 is expressed in terms of “instrumental magnitude”  $m \equiv -2.5 * \log_{10}(\text{counts/sec})$ , both in an absolute sense and relative to the aperture with

60-pixel radius. The latter values are typically called “aperture corrections” and are listed in the column with header  $\langle m - m_{60} \rangle$ . Table 2 also includes values for the observed scatter among the X and Y coordinates of the individual exposures (in pixels).

**Table 2: Mean properties of photometric growth curve for PSA/MIRRORA mode, using Solar-analog star P330E as target. See text for details.**

Aperture Radius (pixels)	$\langle m \rangle$	$\langle m - m_{60} \rangle$ (aperture correction)	Poissonian RMS	Scatter RMS	$\delta X$ RMS (pixels)	$\delta Y$ RMS (pixels)
0.5	-4.318	2.391	0.019	0.223	0.30	0.16
1.0	-5.333	1.376	0.012	0.173	0.30	0.16
2.0	-6.000	0.709	0.009	0.093	0.30	0.16
3.0	-6.251	0.458	0.008	0.032	0.30	0.16
5.0	-6.408	0.301	0.007	0.009	0.30	0.16
7.0	-6.478	0.231	0.007	0.012	0.30	0.16
10.0	-6.540	0.169	0.007	0.008	0.30	0.16
20.0	-6.637	0.072	0.007	0.007	0.30	0.16
40.0	-6.696	0.013	0.007	0.006	0.30	0.16
60.0	-6.709	0.000	0.006	0.007	0.30	0.16

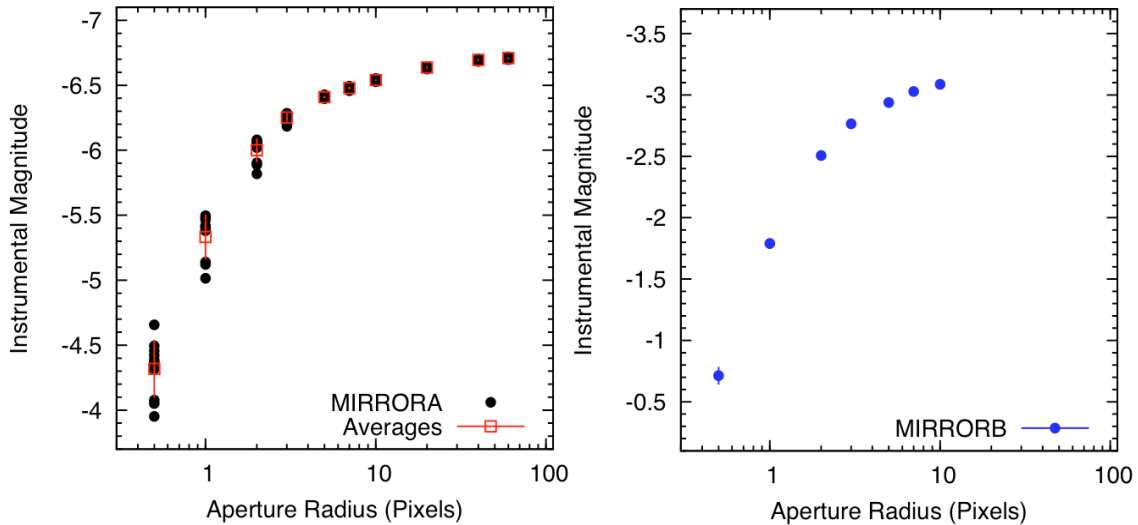


**Figure 4.** Photometric growth curve for PSA imaging measurements of target P330E. The left panel shows all individual measurements for MIRRORA in black and average measurements at each aperture radius in red (along with a  $1\sigma$  error bar). Note the significant scatter at small aperture radii, which are due to focus variations during the HST orbit (cf. below). The right panel shows the MIRRORB measurements along with their (very small)  $1\sigma$  Poisson uncertainties (only one image was taken in MIRRORB). Both panels use the same relative scale in the ordinate to facilitate direct comparison.

As listed in Table 2 and depicted in Figure 4, the 1-sigma value of the photometric scatter among individual (in this case PSA/MIRRORA) exposures is more than 3 times the Poissonian RMS for aperture radii  $< 5$  pixels (equivalent to  $\sim 0.1$  arcsec). This

effect is due to the changing PSF of HST in the presence of thermal changes during the orbit, as shown below.

#### *PSF size versus HST Focus*

To investigate the influence of the HST focus in the context of the observed scatter in the photometry through small measurement apertures, we had the Telescopes Group in the Instruments Division at STScI create a focus model simulation for the optical telescope assembly (OTA) of the HST during the orbits in which the exposures of visit 1 of program 11473 (i.e., the P330E exposures) were taken. The simulated focus values are plotted as a function of time in Figure 5 along with measured FWHM values of the images taken at the center of the COS aperture. The latter values were calculated by means of a 2-D Gaussian fit. Note the clear relation between the focus and the FWHM values, even though there are a few outliers. Quantitatively, the FWHM of the PSF is well approximated by the following function:

$$FWHM = 0.100 * Focus + 1.553 \quad (\text{RMS error} = 0.129 \text{ pixels})$$

where *FWHM* is in pixels and *Focus* is in microns. This function may be useful to approximate PSF sizes with COS when simulated OTA focus values are available. Note however that this function may not be valid outside the range of values measured here.

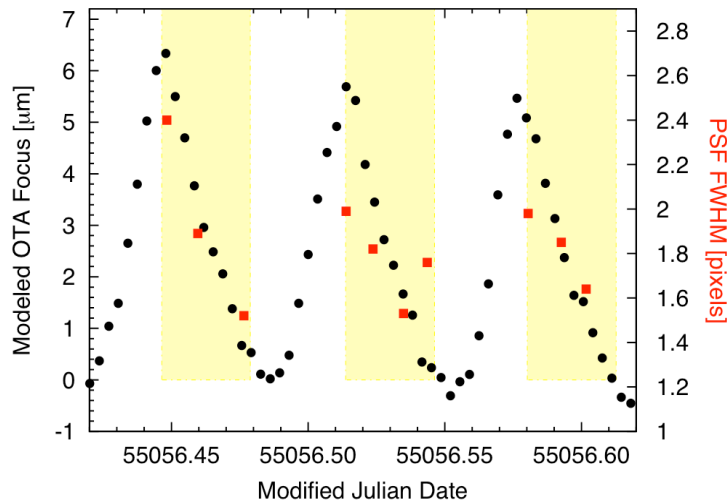


**Figure 5.** The relation between HST focus values and COS PSF size during visit 1 of COS SMOV program 11473. Black circles represent simulated HST OTA focus values (in microns of secondary mirror offset, see values on left-hand ordinate) while red squares represent PSF FWHM measurements at the center of the COS aperture (in pixels, see values on right-hand ordinate). The time intervals shaded in yellow indicate the parts of the HST orbits during which the observations occurred.

#### *Total throughput curves for PSA/MIRRORA and PSA/MIRRORB*

To determine “total” magnitudes and count rates for the MIRRORB data, we used the observation that the shape of the growth curves for MIRRORA and MIRRORB



data are consistent with each other (to within the  $1\sigma$  uncertainties) out to a radius of 10 pixels (see Figure 4). Hence we multiplied the measured MIRRORB count rates in the 10-pixel radius aperture by the average ratio between the 60-pixel and 10-pixel count rates of the MIRRORA measurements to yield “total” MIRRORB count rates. The total count rates found for P330E and LDS749B in the MIRRORB configurations were compared with predictions based on the May 2008 versions of the MIRRORB throughput curve using `synphot` within `IRAF` (these predictions were based on measurements done during COS ground calibration). The results are listed in Table 3.

We found that the predicted count rates for MIRRORB included counts from both the primary and the secondary image rather than only from the primary image. This was addressed by first determining the ratio of counts from the secondary vs. the primary images for the MIRRORB images of P330E and LDS749B. This ratio was found to be  $0.44 \pm 0.01$  as calculated from the measurements with 10-pixel aperture radius. This ratio was accounted for in the last column of Table 3.

**Table 3: Observed vs. predicted count rates for the two target flux standard stars.**

Target Star	PSA/MIRRORA		PSA/MIRRORB		
	observed count rate	obs./predicted ratio	observed count rate	obs./predicted ratio	<i>Corrected</i> obs./pred. ratio
P330E	$482.8 \pm 3.1$	$1.22 \pm 0.01$	$20.1 \pm 0.2$	$0.716 \pm 0.008$	$1.031 \pm 0.011$
LDS749B	...	...	$259.3 \pm 1.7$	$0.657 \pm 0.004$	$0.946 \pm 0.006$

Note that the ratio of observed/predicted count rates is significantly larger for P330E than for LDS749B (an  $8\sigma$  effect). Since P330E has a much “redder” SED than LDS749B, this indicates a higher red sensitivity than that given by the May 2008 throughput curves.

Revised throughput curves were determined as follows. Between 1248 and 2998 Å, the shapes of the May 2008 version of the throughput curves were directly adopted as they were determined from sensitive Thermal Vacuum measurements on the ground. For wavelengths longer than 2998 Å, we multiplied the May 2008 throughput curve of MIRRORB by a wavelength-dependent scale factor that is unity at 2998 Å and has a spectral shape that yields a ratio of predicted count rates for P330E vs. LDS749B which is equal to the observed ratio. The shape of the wavelength-dependent scale factor  $f$  was determined by considering the following parametrization:

$$f(\lambda) = R_{\text{OBS}} / [S_{\text{MIRRORB}}(\lambda) S_{\text{OTA}}(\lambda)] = a R_{\text{SED}}(\lambda)$$

where  $R_{\text{OBS}}$  is the observed ratio of the count rates of P330E and LDS749B for the observing mode in question (i.e., PSA/MIRRORB),  $S_{\text{MIRRORB}}$  is the (May 2008 version of the) throughput curve of MIRRORB,  $a$  is a scale factor,  $R_{\text{SED}}$  is the ratio of the intrinsic SEDs of P330E and LDS749B, and  $S_{\text{OTA}}$  is the throughput curve of the HST.

The resulting value for the scale factor  $a$  was 0.329. For MIRRORA, we adopted the scale factor  $f$  as for MIRRORB. Finally, the resulting throughput curves for MIRRORA and MIRRORB were normalized by (wavelength-independent) scale factors to yield the observed count rates for P330E and LDS749B after convolving them with  $S_{\text{OTA}}$ . The resulting mirror throughput curves are depicted and compared with the May 2008 versions in Figure 6 (both in linear and logarithmic throughput scales). The new mirror throughput curves have been installed in `synphot` as of October 7<sup>th</sup>, 2009, and are hence used in the COS imaging and imaging target acquisition exposure time calculators (ETCs) for Cycle 18 of HST.

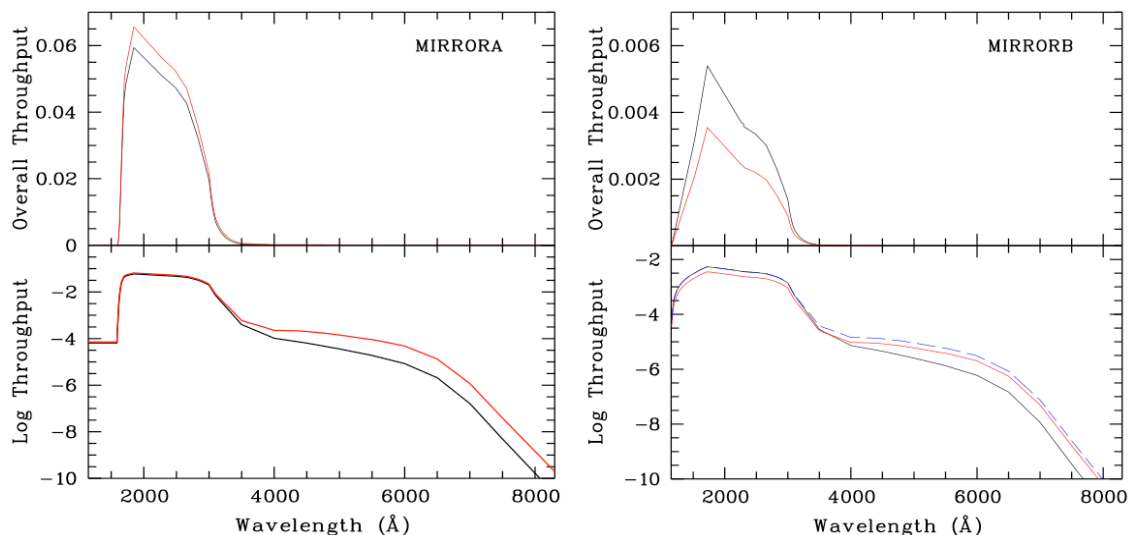


**Figure 6.** *Left panel:* The black line shows the pre-flight throughput curve for COS PSA/MIRRORA. The red line shows the newly derived throughput curve for MIRRORA as explained in the text. The curves shown here are end-to-end throughputs for the COS instrument, but do not include the contribution from the OTA. *Right panel:* Similar to left panel, but for MIRRORB. Note the significantly lower throughput values for wavelengths < 2998 Å in the new throughput curve, which is due to the fact that the pre-flight values included the secondary peak in MIRRORB images whereas the new curve does not. For illustration and comparison purposes, the blue dashed line depicts the old throughput curve to which only the new adjustment for wavelengths > 2998 Å is applied.

## 5.2. Photometry and Image Quality as function of position within the aperture

Due to the combination of the wide wings of the COS PSF (cf. § 4) and the size of the PSA aperture (radius of 1.25 arcsec), the light received from a point source gets diminished when the target is placed away from the center of the PSA aperture. This effect is depicted in Figures 7 and 8. Figure 7 shows the flux received within a measurement aperture of 10 pixel radius (relative to that in the average exposure at the center of the PSA) at each location at which exposures were taken during the SMOV

program. The left panel in Figure 8 shows the values in Figure 7 after averaging the relative flux values along 180° of azimuth, while the right panel compares full growth curves at different distances from the aperture center. The values in Figure 7 can be used to evaluate a photometric correction for point sources located away from the center of the aperture. Note that (1) photometry is not significantly affected within about 0.25 arcsec from the center, (2) light is still received when the target is placed outside of the PSA aperture. The latter is due to the fact that the PSF at the aperture is extended due to the spherical aberration of the OTA.

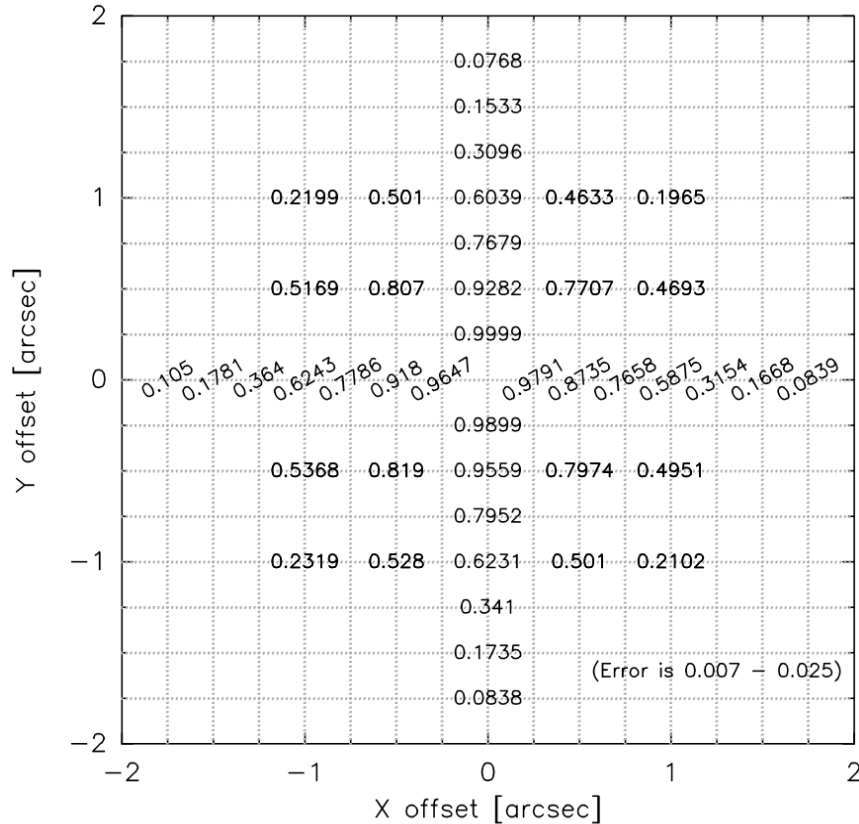


**Figure 7.** Relative throughput as function of spatial offset from the PSA aperture center for point source P330E, as measured from aperture photometry with 10 pixel radius. Typical uncertainties are mentioned at the bottom right of the figure.

To quantify the degradation of the image quality incurred when the target is placed away from the center of the COS aperture, we measured the RMS spot size for each image shown in Figure 7. The RMS spot size  $\Gamma$  is a model-independent measure of the size of an image spot and is defined as follows:

$$\Gamma = \sqrt{\frac{1}{N} \sum_{x,y} [(x - x_0)^2 + (y - y_0)^2] f(x, y)}$$

where  $f(x,y)$  is the image and  $(x_0, y_0)$  are its central coordinates.  $\Gamma$  as a function of spatial offset from the COS aperture center is shown in Figure 9.

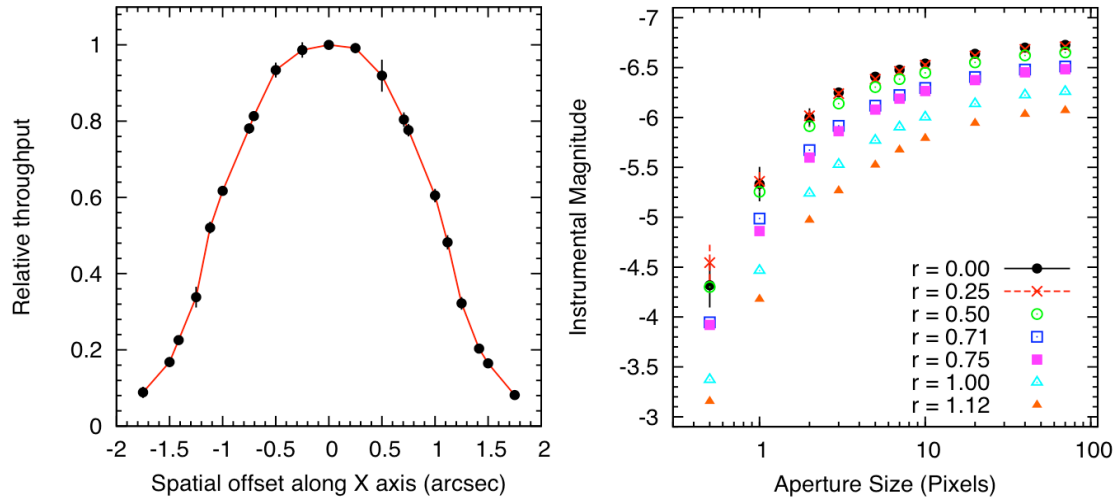


**Figure 8.** *Left panel:* Throughput as function of spatial offset from the aperture center for target point source P330E. This figure was derived by averaging the values in Figure 6 within  $180 < \text{position angle} < 0$  (negative X values) and  $180 < \text{position angle} < 360$  (positive X values). *Right panel:* Photometric growth curve for PSA/MIRRORA as function of spatial offset from the aperture center (see legend for the symbols). Error bars are plotted only for the two innermost positions for clarity considerations.

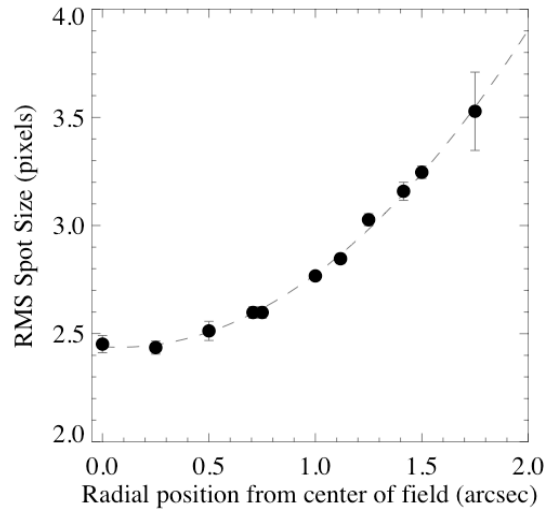
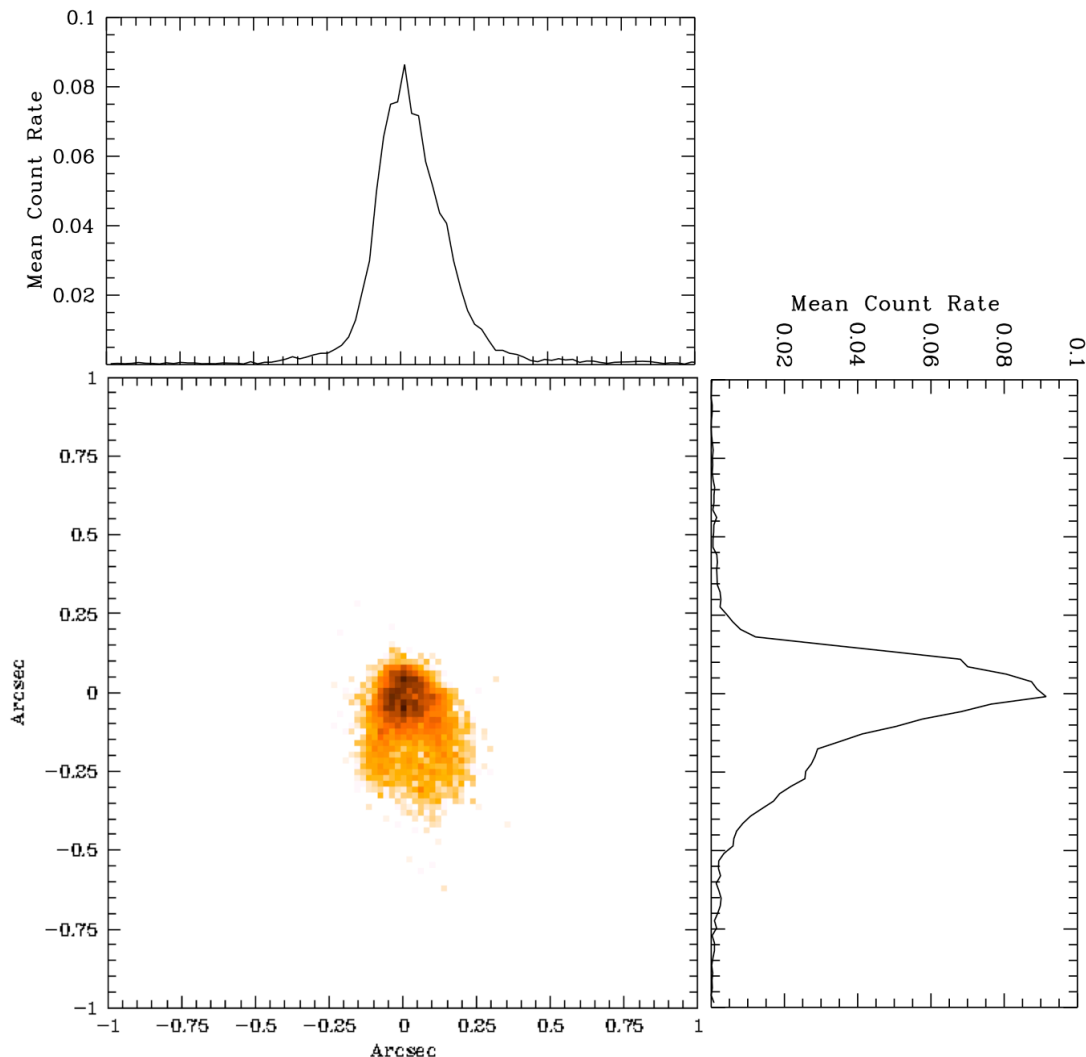


**Figure 9:** Image quality (as measured by RMS spot size) as function of spatial offset from the COS aperture center. The dashed line represents a parabolic fit to the data.

### 5.3. Photometry with the BOA Aperture

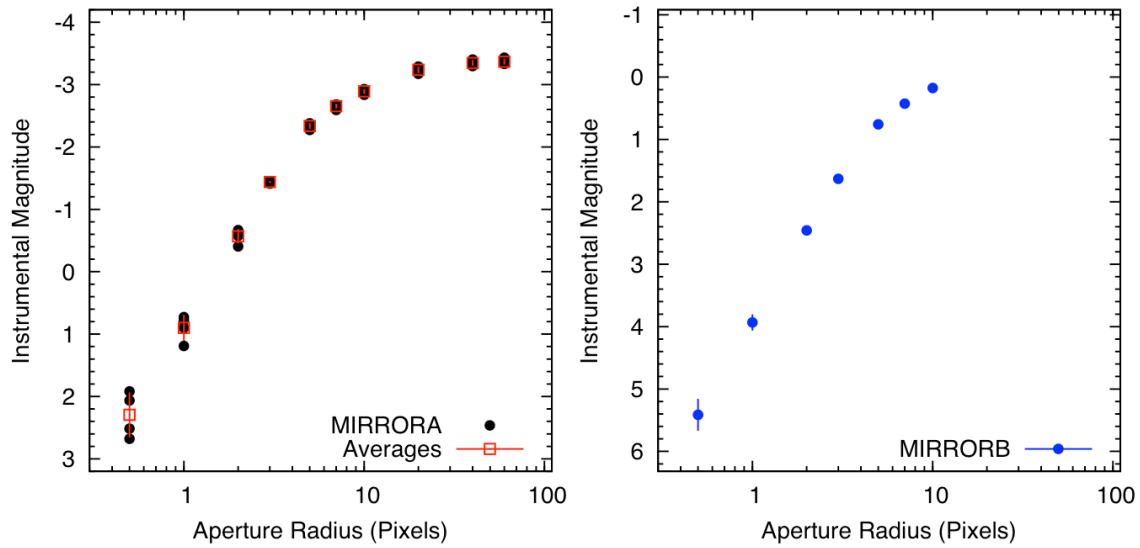
A typical image of a point source observed at the center of the BOA aperture is shown in Figure 10, along with collapsed profiles along the x and y axes. It is obvious that

image quality with the BOA is significantly degraded relatively to the nominal PSA aperture. Hence, it is foreseen that its main purpose will be target acquisition of bright objects (see, e.g., Penton & Keyes 2010). However, a full photometric growth curve is provided below to allow users to derive NUV fluxes for their (bright) targets imaged with the BOA using, e.g., ACQ/IMAGE exposures.



**Figure 10.** The square panel shows the central 2 x 2 arcsec<sup>2</sup> of a combination of 4 aligned BOA/MIRRORA images of a point source at the center of the aperture. The top and right panels show the mean profiles along the x and y axes of the image, respectively.

Results of the growth curve analysis for all (4) exposures of target LDS749B taken at the nominal center of the BOA aperture are shown in Figure 11 and Table 4, in the same formats as those for the PSA data in §5.1 above. Note that the scatter among the magnitudes of the individual BOA exposures is never significantly larger than the Poissonian uncertainties, consistent with the blurred character of images in BOA mode.



**Figure 11:** Photometric growth curve for BOA point source images of target LDS749B. The setup of the two panels is otherwise identical to that in Figure 4.

**Table 4: Mean properties of photometric growth curve for BOA/MIRRORA mode, using LDS749B as target.**

Aperture Radius (pixels)	$\langle m \rangle$	$\langle m - m_{60} \rangle$ (aperture correction)	Poissonian RMS	Scatter RMS	$\delta X$ RMS (pixels)	$\delta Y$ RMS (pixels)
0.5	2.294	5.663	0.353	0.361	1.00	0.41
1.0	0.899	4.267	0.185	0.115	1.00	0.41
2.0	-0.568	2.800	0.094	0.018	1.00	0.41
3.0	-1.439	1.929	0.062	0.042	1.00	0.41
5.0	-2.337	1.031	0.042	0.048	1.00	0.41
7.0	-2.654	0.714	0.036	0.041	1.00	0.41
10.0	-2.891	0.477	0.032	0.039	1.00	0.41
20.0	-3.236	0.132	0.028	0.054	1.00	0.41
40.0	-3.346	0.022	0.026	0.047	1.00	0.41
60.0	-3.368	0.000	0.026	0.046	1.00	0.41

#### 5.4. Summary of Relative Throughputs of Imaging Modes

Table 5 summarizes the relative throughputs of the various imaging modes as measured from the images located in the center of the PSA or BOA aperture. Throughput values refer to a radius of 60 pixels, and are listed for targets P330E and LDS749B when both are available for the mode in question. The value for LDS749B in PSA/MIRRORA mode is rendered in italic font to indicate that it was determined indirectly, i.e., by using the updated throughput curves described in §5.1 above.

**Table 5: Relative Throughputs of COS Imaging Modes.**

Aperture	MIRROR	Relative Throughput	
		P330E	LDS749B
PSA	MIRRORA	1.000	<i>1.000</i>
PSA	MIRRORB	$(4.16 \pm 0.05) 10^{-2}$	$(5.01 \pm 0.15) 10^{-2}$
BOA	MIRRORA	---	$(4.35 \pm 0.13) 10^{-3}$
BOA	MIRRORB	---	$(2.58 \pm 0.07) 10^{-4}$

## 6. Image Drift During 5 Orbits of Data Taking

Pre-flight tests of COS showed some drift of the Optical Select Mechanisms (OSMs) after being stopped in their nominal positions. As this affects imaging observations as well as spectroscopic ones, we quantified this drift during the observations described here by means of the WCA (Wavelength Calibration Aperture) exposures listed in Table 1. The result is depicted in Figure 12. The drift is dominated by movement in the X direction ( $\sim 3.5$  pixels maximum), and is most likely due to the settling of the grating/mirror rotation mechanism. As shown in Fig. 12, the behavior of the drift is well fit by two exponential decays giving a characteristic size and time scale. This is likely due to the fact that two rotating mechanisms are involved. The overall maximum drift in X is about 3.5 pixels with an e-folding time of  $\sim 50$  min. In comparison, the drift in the Y direction is found to be much smaller: An exponential fit yields about 0.76 pixels of drift over a time scale of 1.3 hours. Given the significant amplitude of the image drift and its time scale, *observers using imaging exposures longer than about 200 s are urged to use the TIME-TAG operating mode with the FLASH optional parameter* (see the Phase II Proposal Instructions for the COS instrument). This mode takes short WCA exposures during a time-tagged exposure, enabling one to follow the drift accurately. This will allow one to retain the best possible imaging performance during long exposures.

## 7. Image-mode Plate Scale and Orientation

Plate scale and orientation for imaging mode was determined by means of an IDL-based program which finds image centroids using the algorithm implemented in the flight software that performs COS image-mode target acquisitions. These centroids were measured only for exposures with spatial offsets  $\leq 0.5$  arcsec from the aperture center (the irregular morphology of spots further away from the aperture center cause the centroid to be less accurate). After correcting for the drift as determined from the WCA exposures (see previous section), the plate scale was determined to be  $42.5 \pm 0.2$  pixels/arcsec or  $0.0235 \pm 0.0001$  arcsec/pixel, both in X and Y directions.

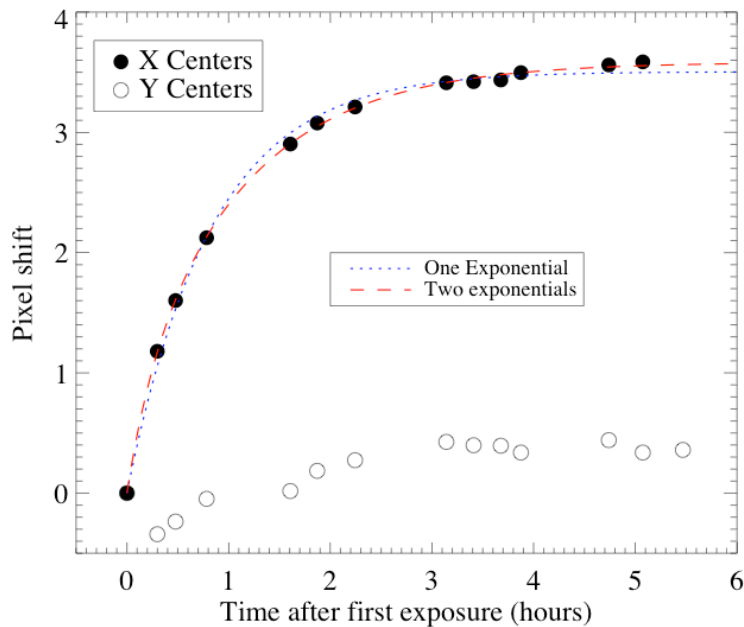


**Figure 13:** Image drift in X and Y directions as a function of time. See legend for symbols and line types. The drift is dominated by movement in the X direction, and its behavior is fit accurately by a (double) exponential curve.

To determine the rotation angle of spatial offsets relative to the commanded offsets, we used all exposures with commanded offsets in X equal to zero and fitted a line to the drift-corrected centroids. This yielded a rotation angle of  $0.52 \pm 0.01$  degrees from vertical, with larger offsets in Y associated with larger offsets in X.

## Change History for COS ISR 2010-10

Version 1: 11 March 2010 - Original Document

Version 2: 7 October 2010 – Fixed numerical values in the FWHM equation on page 8

## References

- Bohlin, R. C., Riess, A., & de Jong, R., 2006, Instrument Science Report NICMOS 2006-002 (Baltimore: STScI)
- Bohlin, R. C., Harris, A.W., Holm, A.V., & Gry, C., 1990, ApJS, 73, 413
- Bohlin, R. C., & Koester, D., 2008, AJ, 135, 1092
- Colina, L., & Bohlin, R. C., 1996, AJ, 113, 1138
- Colina, L., Bohlin, R. C., & Castelli, F., 1996, AJ, 112, 307
- Ghavamian, P., et al. 2009, Instrument Science Report COS 2009-01 (Baltimore: STScI)
- Krist, J. E., & Burrows, C. J. 1995, Applied Optics, 34, 4951



Penton, S., & Keyes, C. D. 2010, Technical Science Report COS 2010-03 (Baltimore: STScI)  
Woods, T. N., et al. 1996, J. Geophys. Res., 101(D6), 9541

## **Acknowledgements**

We acknowledge relevant discussions with Tony Keyes, Parviz Ghavamian, and Ed Smith.